Polymer 100 (2016) 111–118

Contents lists available at ScienceDirect

Polymer

journal homepage: www.elsevier.com/locate/polymer

Interfacial interaction enhancement by shear-induced β-cylindrite in isotactic polypropylene/glass fiber composites

Yijing Qin [a], Yahu Xu [a, 1], Liying Zhang [a], Guoqiang Zheng [a, *], Xingru Yan [b], Kun Dai [a], Chuntai Liu [a], Changyu Shen [a, **], Zhanhu Guo [b, ***]

[a] School of Materials Science and Engineering, The Key Laboratory of Material Processing and Mold of Ministry of Education, Zhengzhou University, Zhengzhou 450001, PR China

[b] Integrated Composites Laboratory (ICL), Department of Chemical & Biomolecular Engineering, University of Tennessee, Knoxville, TN 37996, USA

ARTICLE INFO

Article history:
Received 14 June 2016
Received in revised form
2 August 2016
Accepted 4 August 2016
Available online 5 August 2016

Keywords:
Interfacial crystallization
β-Cylindrite
Mechanical properties

ABSTRACT

Isotactic polypropylene (iPP)/glass fiber (GF) composites with different specific interfacial features (*viz.*, α-spherulite, α-cylindrite and β-cylindrite) were prepared via shear-induced interfacial crystallization. α-spherulite, α-cylindrite and β-cylindrite were successively encouraged at the interface between iPP matrix and GF with increasing the fiber-pulling speed. Moreover, the composite specimens containing β-cylindrite exhibited remarkably higher interfacial shear strength (IFSS) than those containing α-spherulite or α-cylindrite, as demonstrated by the single fiber fragmentation test (SFFT). More interestingly, simultaneously improved tensile strength and toughness were observed in the presence of β-cylindrite. This study offers a new insight that β-cylindrite produced by shear is an alternative approach to achieve comprehensive mechanical properties for the iPP/fiber composite systems.

1. Introduction

The past few decades have witnessed an intense growth of polymer/fiber composites in many fields, such as automobiles, aerospace, military and sports goods, *etc*., due to their excellent comprehensive properties. Millions of tons of polymer/fiber composites are consumed in various applications each year. Apart from homogeneous dispersion of fibers in polymer matrix, strong interfacial interaction between rigid fiber and soft matrix plays another crucial role in obtaining high-performance composites [1]. Interfacial crystallization has been recognized as a promising method to improve polymer/fiber interfacial interactions. For example, transcrystallinity (TC, heterogeneous nucleation [2]) and cylindrite (self-nucleation [3,4]) as two important kinds of interfacial crystallization have attracted increasing attention in recent years.

Intrigued by creating desirable interfacial properties of high-performance composites, many researchers have devoted themselves to revealing the underlying roles of interfacial crystallization in the polymer/fiber composite systems. To date, the influences of crystallinity [5,6], chemical activity of fiber surface [7,8], wetting and de-wetting [9], thickness of the transcrystalline layer [10,11] on the interfacial enhancement have been discussed. Unfortunately, it is still a controversy whether the interfacial crystallization can improve the interfacial adhesion [6,11–15].

Among semicrystalline polymers, isotactic polypropylene (iPP) has been intensively investigated as a representative polymer containing polymorphic modifications. Among them, α-form crystal, generally developed via melt crystallization under static condition, is the most thermodynamically stable crystal and possesses relatively good mechanical performance. Nevertheless, its impact strength is very poor especially at low temperatures [16]. With respect to β-form crystal, it can be abundantly obtained through some special crystallization processes, such as in a thermal gradient [17], shearing or elongation of melt during crystallization [16,18–22], with special nucleating agents during bulk crystallization [23–26]. Although the β-form crystal is a thermodynamically metastable phase, it has some advantages over its α-counterpart, such as improved elongation at break and impact toughness [26]. The interfacial crystallization kinetics was reported to be promoted

* Corresponding author.
** Corresponding author.
*** Corresponding author.
E-mail addresses: gqzheng@zzu.edu.cn (G. Zheng), shency@zzu.edu.cn (C. Shen), zguo10@utk.edu (Z. Guo).

[1] The author Yahu Xu contributed equally to this work and should be considered as co-first authors.

http://dx.doi.org/10.1016/j.polymer.2016.08.016
0032-3861/

by the presence of interfacial shear stress, and two shear stress thresholds existed for the development of two different crystal modifications of iPP (*viz.*, α- and β-form crystals) [27]. Furthermore, an interfacial sheath structure produced at higher fiber-pulling speeds was demonstrated to induce the formation of β-cylindrite effectively [28]. The relationship between mechanical properties and different interfacial crystal modifications has not received any attention and is another issue related to the interfacial adhesion.

In this work, single glass fiber (GF)/iPP composite specimens were prepared containing specific types of interfacial crystal modification. The single fiber fragmentation test (SFFT) was employed to investigate the interfacial adhesion in the iPP/GF composite systems. The tensile test was carried out to measure the tensile strength and toughness. The effects of interfacial morphology, especially crystal modification of interfacial crystalline layer, on the interfacial interaction were systematically studied and analyzed.

2. Experimental

2.1. Materials

Commercial iPP granules (T30S) were supplied by Lanzhou Petroleum Chemical Co., Ltd, with a melting flow index of 2.6 g/10 min (190 °C, 21.6 N load), and $\overline{M}_n$ of 11.0 × 10^4 g/mol. The GFs utilized were E-glass fibers with an average diameter of *ca.* 14 μm, supplied by Zhengtong Chemical Industry Co., Ltd. The GFs were rinsed several times with acetone and deionized water successively with ultrasonication to remove the sizing agent, then dried in a vacuum oven at 80 °C for 10 h.

2.2. Specimen preparation

Thin iPP films were previously prepared by hot compression-molding iPP granules at 200 °C. A single GF was first sandwiched between two pieces of iPP thin films. The sandwiched specimen was pressed at 180 °C for 3 min and then transferred to hot stage (Linkam THMS 600). Afterwards, as depicted in Fig. 1A, the specimen was heated to 200 °C for 5 min to erase the possible thermo-mechanical history effect and then cooled down to 134 °C at a cooling rate of 20 °C/min. Once the temperature reached 134 °C, the fiber was pulled along the fiber's longitudinal axis for 15 s at a preset speed of 0, 30 and 150 μm/s by an improved fiber-pulling device. The operating principles of this fiber-pulling device have been reported previously [27]. Briefly, the major part of this pulling device is a stepping motor with a precise planetary gear reducer. Meanwhile, screw rod and guide rail are used to change rotary motion into linear motion, and a fiber-fixing device is integrated to the guide rail assembly to fasten the fiber. Subsequently, isothermal crystallization was performed for the preset crystallization time (0, 8, 16 and 24 min) at the same temperature of 134 °C. For the sake of brevity, isothermal crystallized specimens were labeled as iPP-0, iPP-30 and iPP-150, where 0, 30 and 150 represented the fiber-pulling speed.

2.3. Polarized optical microscopy (POM)

To study the interfacial morphology between iPP matrix and GF, an Olympus BX51 POM equipped with a PixeLINK PL-A662 CCD was employed to trace and record the evolution of interfacial morphology during the isothermal crystallization process.

2.4. Polarized Fourier transform infrared spectroscopy (FTIR)

To investigate the iPP chain orientation level of interfacial crystalline layer close to the GF surface of specimens isothermally crystallized for 24 min, FTIR equipped with a polarizer (NICOLET 6700) was used here. The spectra were recorded from 400 to 4000 cm^{-1} with a resolution of 4 cm^{-1}.

2.5. Differential scanning calorimetry (DSC)

The melting behaviors of specimens isothermally crystallized for 24 min were characterized using a TA 2920 Modulated DSC with nitrogen as purge gas. For each measurement, the measured specimen cut from original specimen symmetrically along the fiber axis with a width of 1 mm (including the whole interfacial crystalline layer) was heated from 30 to 200 °C at a heating rate of 10 °C/min.

It should be pointed out that all the measured specimens in the FTIR and DSC measurements were quenched, and were prepared by quickly transferring the crystallized specimens into ice water mixture to preserve their crystalline morphologies.

2.6. Single fiber tensile strength test

A single GF was held in a miniature tensile tester (Linkam TSTE350) at a declining rate of 0.01 mm/min. The gage lengths were 2.5, 5, 7.5, 10, 12.5 and 15 mm, respectively. The tensile strength of GF with different gage lengths was recorded.

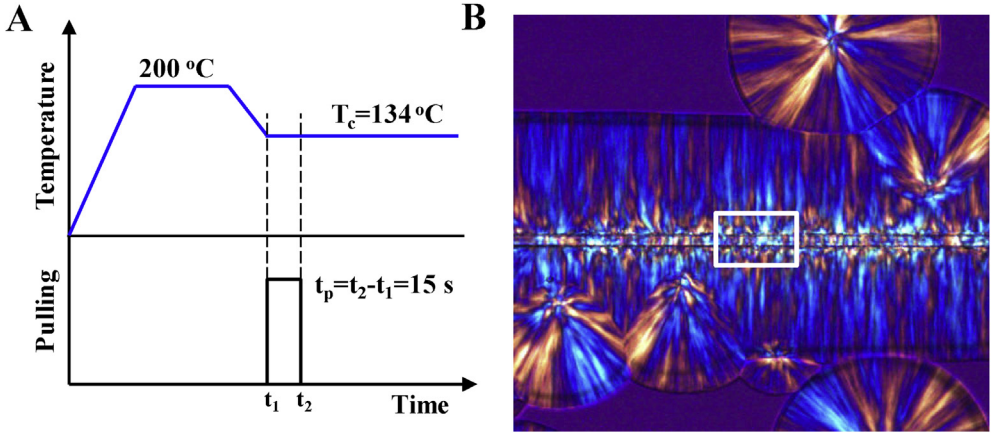

Fig. 1. Schematic representations of the applied thermo-mechanical history (A) and the detected region for FTIR spectra test (white rectangle) (B).

2.7. Single fiber fragmentation test (SFFT) and tensile test

The specimens crystallized isothermally for 0, 8, 16 and 24 min were quenched immediately into ice water mixture for SFFT. All the specimens were cut into rectangular geometry (16 mm × 1 mm). It should be noted that the rectangular specimens fully contained total interfacial crystalline layers. The SFFT was carried out using a Suns tensile tester (UTM2203, Shenzhen Suns Technology Stock Co., Ltd, China) with a load cell of 100 N at a crosshead rate of 1.0 mm/min. This test was performed at around 25 °C. During each test, a specimen was stretched to 20% strain, beyond which the fiber would not continue to fracture. At least ten specimens for each condition were measured. After SFFT test, the specimens were observed by POM to measure the fragmentation length. To further investigate the effect of interfacial morphology, especially crystal modification on the interfacial enhancement, the tensile test of specimens isothermally crystallized for 24 min was performed. The test conditions were the same as those used during SFFT. At least five specimens for each condition were tested and the average values were reported.

3. Results and discussion

3.1. Influence of shear on interfacial morphology and crystal modification

Fig. 2 shows the POM images of interfacial morphology at different time during isothermal crystallization. For comparison, the interfacial morphology developed under static condition (*i.e.*, fiber-pulling speed is 0 μm/s) is also presented (see Fig. 2A). Expectedly, GF exhibits no nucleation ability towards iPP in quiescent melt, so only sporadic spherulites are randomly distributed in the matrix, consistent with previous reports [20,21,27–29]. In the case of lower pulling speed (30 μm/s), Fig. 2B, the interfacial morphology turns out to be significantly different from that of the static one. A thin layer of flocculent coating structure is observed to appear on the GF surface at the end of fiber-pulling (see the enlarged view in Fig. 2B, 0 min). In fact, once the shear field is applied on the polymer melt, the orientation level of polymer chains in the interfacial region between GF and iPP matrix is inevitably enhanced. Such oriented iPP chains (proved by the following FTIR measurement) will preferentially occur along the GF axis and thus can act as nuclei for iPP crystallization. Once the surface of GF is completely occupied by the growing crystals, these crystals are restricted to grow perpendicular to the GF axis direction and gradually form cylindrite covering the GF surface [3]. Additionally, the radius of cylindrite increases with increasing the crystallization time (see Fig. 2B, 8 min, 16 min), and finally the radius of cylindrite reaches *ca.* 110 μm at 24 min. Furthermore, the crystal modification of such cylindrite is α-crystal, which can be confirmed by the selective melting experiment as shown in Fig. 3A and A_1. The reason can be understood as follows: the melting point of α-form crystal is about 166 °C [3] (which can be further proved by the following DSC heating curve, Fig. 4), thus α-form crystal can well survive at 158 °C. Considering the fact that GF has no nucleation ability towards iPP under static condition, the α-cylindrite observed here is undoubtedly attributed to the interfacial shear brought by the pulling fiber. As shown in Fig. 2C, even though the fiber-pulling speed is increased to as high as 150 μm/s, the profile of interfacial crystalline layer is somewhat similar to that of iPP-30. It is worth noting that such interfacial cylindrite shows stronger birefringence. Moreover, at the same crystallization time of 24 min, the radius of this bright cylindrite reaches a value of *ca.* 128 μm. As mentioned above, the radius of α-cylindrite in iPP-30 is only *ca.* 110 μm (see Fig. 2B, 24 min), therefore, it can be concluded that such bright cylindrite in iPP-150 is different from its α-counterpart, Fig. 2B. Additionally, the subsequent selective melting experiment shows that such bright cylindrite in iPP-150 will disappear at 158 °C (see Fig. 3B and B_1). Moreover, considering the fact that β-form crystal of iPP with stronger birefringence [30–32] grows faster than its α-counterpart in the temperature range of 100–140 °C and it will be melt at around 158 °C [22,33], this bright cylindrite should

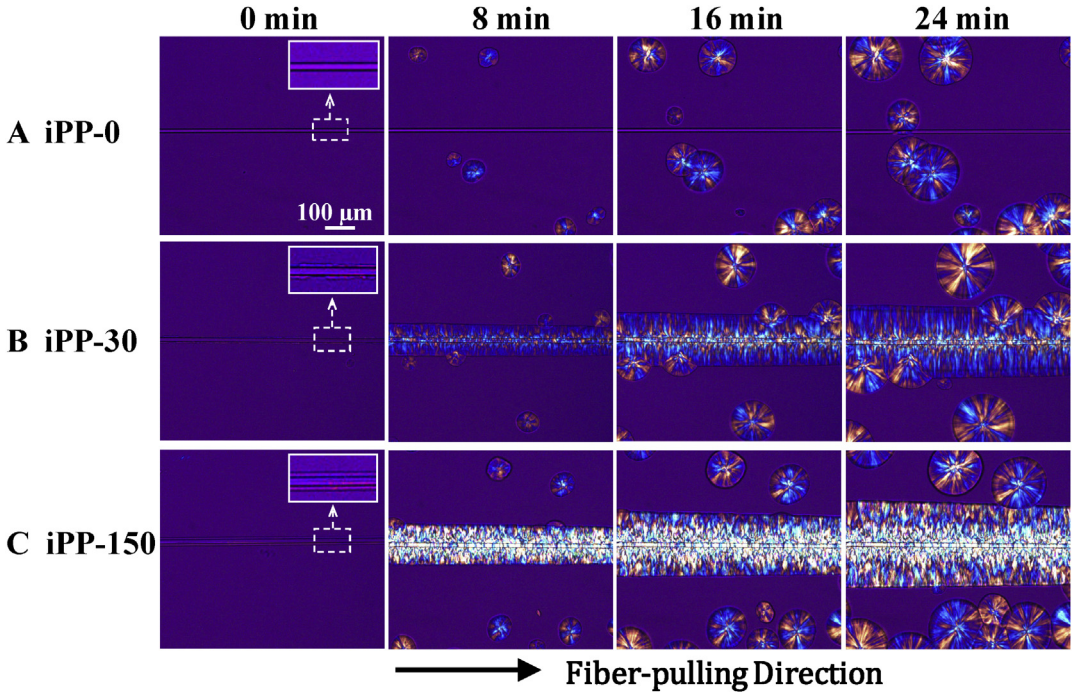

Fig. 2. POM images of the interfacial morphology during isothermal crystallization.

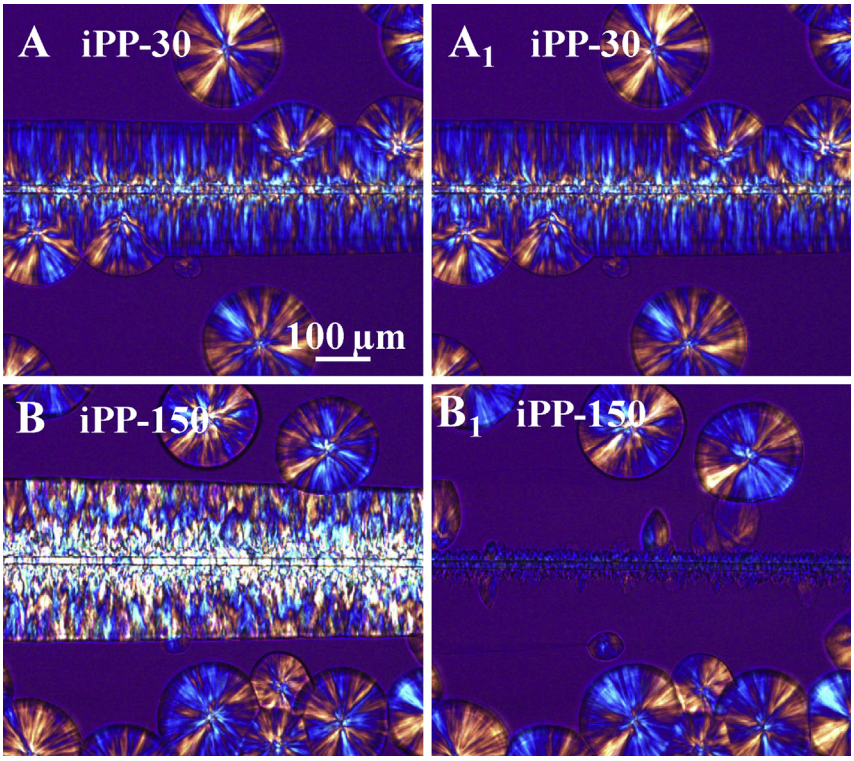

Fig. 3. Interfacial morphology in the isothermally crystallized specimens before (A and B) and after (A_1 and B_1) selective melting experiment at 158 °C.

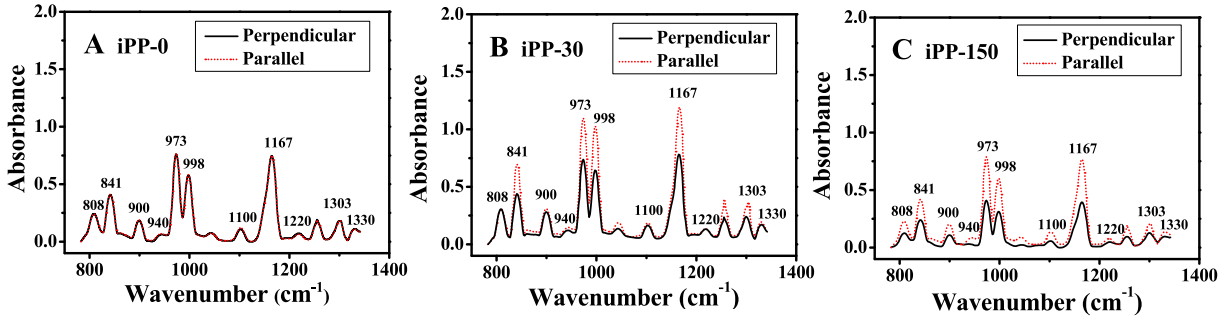

Fig. 4. Polarized FTIR spectra of the interfacial crystalline layers of isothermally crystallized specimens.

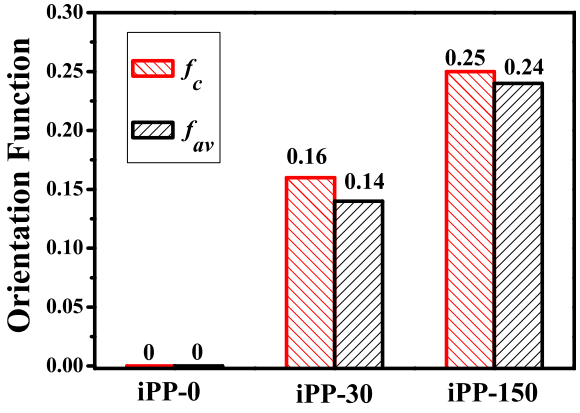

Fig. 5. Calculated orientation function of the interfacial crystalline layers close to GF surface.

be β-form crystal (which is also confirmed by the DSC heating curve, Fig. 6). The above results suggest that the interfacial shear is crucial to determine the development of different crystal modifications.

3.2. Local orientation level of interfacial crystalline layer investigated by FTIR

The above results distinctly demonstrate that the interfacial shear has a significant effect on the crystal modifications of iPP. Here FTIR was employed to characterize the orientation level of interfacial crystalline layers of the isothermally crystallized specimens. The detected region for FTIR test is illustrated by white rectangle in Fig. 1B. Fig. 4 manifests the polarized FTIR spectra of the interfacial crystalline layers in the specimens isothermally crystallized at 134 °C for 24 min. Identical absorbance intensities are observed in the parallel- and perpendicular-polarized FTIR spectra of iPP-0 (see Fig. 4A), suggesting that iPP chains randomly arrange in the absence of shear. Contrarily, for both iPP-30 and iPP-

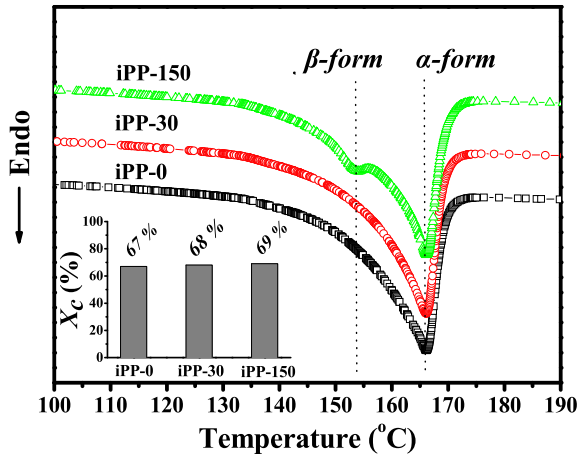

Fig. 6. DSC heating curves of the specimens isothermally crystallized for 24 min at 134 °C. The inset shows the total crystallinity (X_c).

150, the parallel-polarized FTIR spectrum is apparently different from perpendicular-polarized one (see Fig. 4B and C), that is, the intensity of parallel-polarized FTIR spectrum (obtained from the infrared beam polarized parallel to the fiber's longitudinal axis) is dramatically stronger than that of the perpendicular-polarized FTIR spectrum (obtained from the infrared beam polarized perpendicular to fiber's longitudinal axis). This indicates that the iPP chains close to GF surface are principally oriented along the fiber's longitudinal axis (*viz.*, fiber-pulling direction) in iPP-30 and iPP-150.

The Herman's orientation function (f_i), to evaluate the orientation level of a given molecular axis with respect to the sample direction, can be calculated by the following expression [33,34]:

$$f_i = \frac{R-1}{R+2} \tag{1}$$

$$R = \frac{A_{//}}{A_{\perp}} \tag{2}$$

where R is the dichroic ratio, $A_{//}$ is the parallel-polarized infrared absorbance intensity and $A_{\perp}$ is the perpendicular-polarized one for a particular vibration in the observed FTIR spectra. For a polymer without any orientation, R is always equal to 1. While it is a maximum value for a fully oriented polymer, and the maximum value changes with different bands. The dichroic ratios of different FTIR bands for all the samples are summarized in Table 1.

Table 1
Dichroic ratios of different FTIR bands of the interfacial crystalline structure close to GF of resultant isothermally crystallized specimens.

Wavenumber (cm^{-1})	Dichroic ratio (R)		
	iPP-0	iPP-30	iPP-150
940	1.08	1.15	2.59
1220	0.91	0.95	2.36
1167	1.00	1.45	1.78
1303	1.00	1.45	1.93
1330	0.98	1.06	2.40
841	1.00	1.51	1.72
998	1.01	1.58	2.01
900	1.00	1.03	1.83
808	1.00	0.97	2.34
1100	1.02	1.17	1.88
973	1.00	1.47	1.94
1156	1.04	1.09	2.12

Apparently, one can find that all the values of R for iPP-0 is very close to 1, while R for iPP-30 and iPP-150 deviates from 1 to a certain degree. These dichroic ratios preliminary verify that a higher fiber-pulling speed can produce a more remarkable extent of molecular chains orientation.

According to other studies [33–37], the strong band at 998 cm^{-1} is always selected for the orientation function of crystalline phase (*viz.*, f_c) and R will be $(A_{//}/A_{\perp})_{998}$. To measure the average orientation level (*viz.*, f_{av}) that includes both crystalline structure and amorphous phase orientation, the band at 973 cm^{-1} is selected and f_{av} is calculated based on $(A_{//}/A_{\perp})_{973}$ (Painter et al. and Ward attribute this peak to the superposition of two very close peaks, one located at 972 cm^{-1} (crystalline) and the other at 974 cm^{-1} (amorphous) [38,39]). f_c and f_{av} of different specimens calculated based on Equation (1) are displayed in Fig. 5. Both f_c (ranges from 0 to 0.25) and f_{av} (ranges from 0 to 0.24) are observed to increase with increasing the fiber-pulling speed. This evidently proves that a higher interfacial shear (*viz.*, higher fiber-pulling speed herein) facilitates a higher chain orientation level of iPP in the interfacial crystalline layers.

3.3. Crystal modifications and crystallinity investigated by DSC

The crystal modifications of interfacial crystallization can be further verified via the DSC heating curves, Fig. 6. The endothermic peaks at 166 and 154 °C are attributed to the α- and β-form crystals of iPP, respectively [3,22,33]. Furthermore, one can conclude that only α-form crystal exists in iPP-0 and iPP-30, but both α- and β-form crystals are produced in iPP-150. This result is well consistent with the selective melting experiment (see Fig. 3).

The total crystallinity (X_c) was calculated from Equation (3):

$$X_c = \frac{\Delta H_i}{\Delta H_i^m} \times 100\% \tag{3}$$

where ΔH_i is the apparent enthalpy of fusion and ΔH_i^m is the enthalpy of fusion for 100% crystallized iPP, 209 J/g [40]. The calculated X_c is 67, 68 and 69% for iPP-0, iPP-30 and iPP-150 (see the inset in Fig. 6), respectively.

3.4. Influence of interfacial morphology and crystal modification on IFSS

Single fiber tensile strength (σ) is presented in Fig. 7 as a function of different length (L) of single GF, and this straight line represents the result of optimizing linear fitting of these discrete

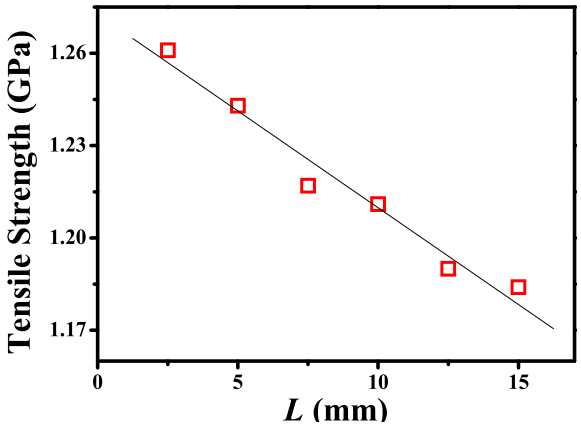

Fig. 7. Tensile strength of single GF with different length (L).

points. The derived linear-fitting Equation (4) is used to calculate the IFSS.

$$\sigma = 1.273 - 0.0063\ L \tag{4}$$

To evaluate the influence of interfacial morphology, especially different crystal modifications on the interfacial properties of iPP/GF composites, SFFT was performed. As well documented [8,11], the tensile load can be transferred from matrix to fiber through the interfacial shear stress. Thus, when axial tensile stress applied on one fiber exceeds the critical failure stress of fiber, the fiber will fracture. With increasing the load, the number of fragmentation will increase and reach a constant owing to the limited fiber length to transfer larger stress to fracture, which is defined as the saturation in single fiber fragmentation process [41].

As expected, the cumulative distribution of fragment length is obtained after SFFT test, Fig. 8. The fragment length cumulative distribution of iPP-0, iPP-30 and iPP-150 isothermally crystallized for the same time is observed to successively shift to left (*viz.*, smaller fragment length), indicating a stronger interfacial adhesion and higher stress transfer efficiency at the interface [7]. Therefore, one can deduce that iPP-150 has the strongest interfacial adhesion and highest stress transfer efficiency in comparison with iPP-0 and iPP-30 prepared under the same conditions. Moreover, the cumulative distribution of all specimens also shows a shift to the left with increasing the isothermal crystallization time. This phenomenon firmly indicates that the interfacial adhesion is strongly controlled by the interfacial crystalline layer.

The IFSS is obtained according to Equation (5) [42]:

$$\tau = \frac{d\sigma_f(l_c)}{2l_c} \tag{5}$$

where τ is interfacial shear strength, l_c is fiber critical effective length, $\sigma_f(l_c)$ is fiber strength at the critical length, d is fiber diameter. The average fiber fragmentation length $\bar{l}$ is determined as Kl_c, where K is a correction factor for orientation of fibers, and usually presumed to be 3/4 [43]. $\bar{l}$ is obtained from the number of fragmentation counted via the observation of POM, *i.e.*, total embedded fiber length divided by the number of fragmentation. Thus, an empirical formula can be deduced and expressed as Equation (6):

$$\tau = \frac{3\sigma_f(l_c)d}{8\bar{l}} \tag{6}$$

The average fiber fragmentation length $\bar{l}$ at the saturation stage is summarized in Table 2. According to Equations (4) and (6), IFSS was calculated. Fig. 9A shows the IFSS as a function of isothermal crystallization time. The iPP-0 is observed to show the lowest strength value, which slightly increases from 2.01 to 2.31 MPa with increasing the isothermal crystallization time from 0 to 24 min. The slightly increased IFSS for iPP-0 is probably derived from the gradually increasing number and size of spherulites developed in the matrix. In other words, longer isothermal crystallization time results in larger crystallinity at the interfacial region of specimens, which is helpful for the slightly increased IFSS of iPP-0.5 The IFSS for iPP-30 and iPP-150 containing cylindrites shows a remarkable increase with increasing the crystallization time. It should be noted that even for iPP-30 and iPP-150 without isothermal crystallization,

Table 2
Average fiber fragmentation length (μm) at the saturation stage.

Specimens	Crystallization time (min)			
	0	8	16	24
iPP-0	3154	3121	2978	2840
iPP-30	2901	2112	1776	1645
iPP-150	2570	1593	1084	994

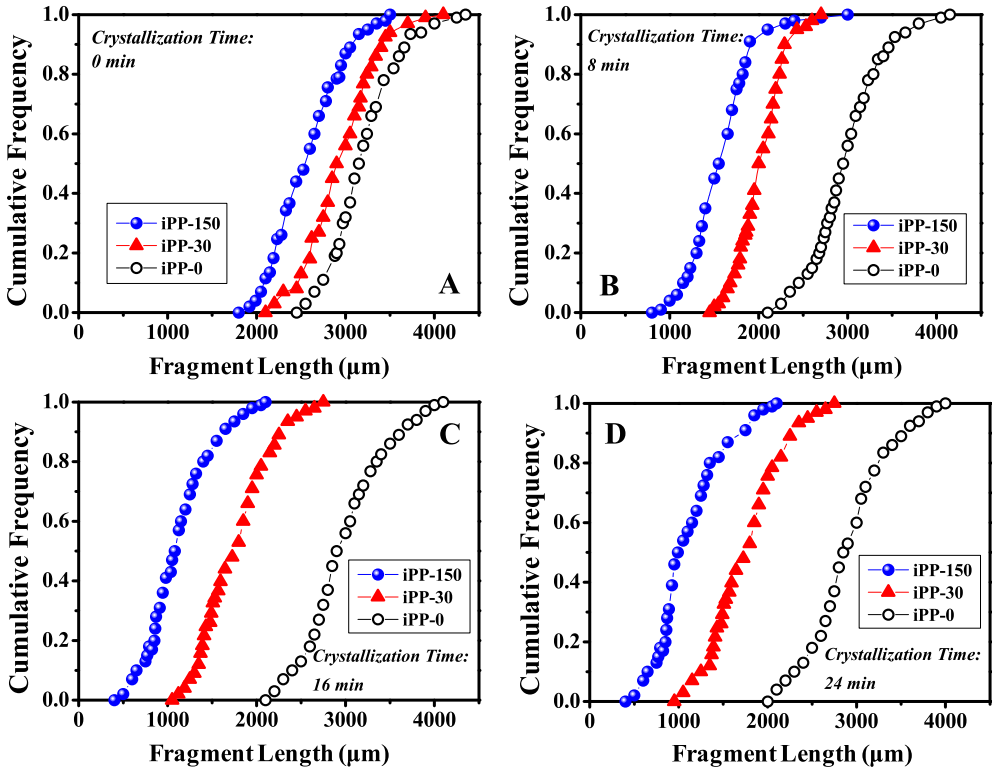

Fig. 8. Cumulative fragment length distribution of isothermally crystallized specimens.

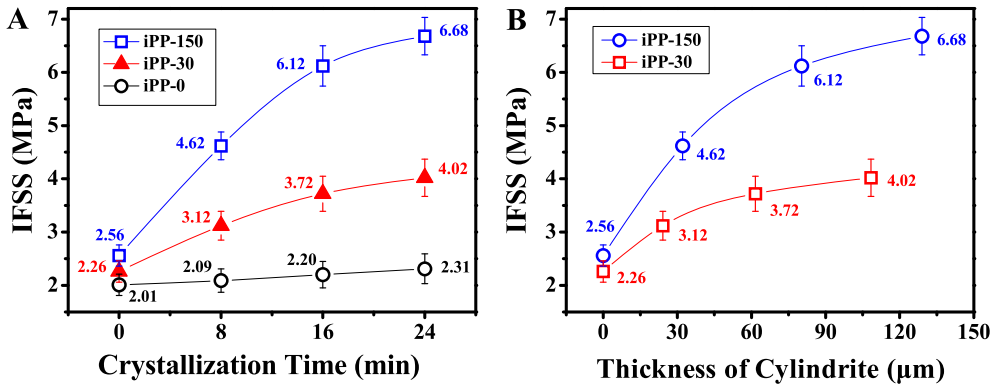

Fig. 9. IFSS as a function of (A) crystallization time and (B) thickness of cylindrite.

the IFSS values are 2.26 and 2.56 MPa, respectively, and still higher than that of iPP-0. This should be attributed to partial preservation of oriented structure in iPP-30 and iPP-150 at the interface upon immediately quenching in ice water mixture after pulling the fiber.

Fig. 9B presents IFSS as a function of the thickness of cylindrite. The IFSS is observed to increase with increasing the cylindrite thickness for both iPP-30 and iPP-150. The IFSS of iPP-30 elevates from 2.26 to 4.02 MPa, with an increase of 78%, while the IFSS of iPP-150 increases from 2.56 to 6.68 MPa, with a sharp increment of 160%. This is well consistent with that the stress transfer efficiency was increased with increasing the thickness of interfacial crystalline layer [44]. It should be also noted that IFSS of iPP-150 is much higher than that of iPP-30 for the same thickness of cylindrites. Combined with the interfacial morphology (Fig. 2) and orientation function (Fig. 5), such an obvious discrepancy may be caused by their different orientation levels at the interfacial crystalline layer close to GF surface as well as different internal microstructures of β- and α-form crystals. These results offer direct evidence that IFSS is not only influenced by the thickness of interfacial crystalline layer but also by the interfacial crystal modification.

Fig. 10 presents the typical micrographs of fiber-matrix failure modes after SFFT. An obvious interfacial debonding is clearly observed with a long empty cylindrical channel in iPP-0 (as indicated by a black arrow), suggesting a weak interfacial adhesion (see Fig. 10A) [5,45]. While for iPP-30 (Fig. 10B), a small gap marked by a black arrow is observed along the fiber/matrix interface, representing a better interfacial adhesion than iPP-0. In contrast, extensive cracks in the direction perpendicular to fiber's longitudinal axis at different breaking points are clearly detected for iPP-150 (see black arrows in Fig. 10C). Obviously, the interfacial adhesion between fiber and iPP-150 matrix is strong and fracture at the interface can efficiently propagate to matrix. In a word, this change of failure mode is a direct reflection of the improvements in

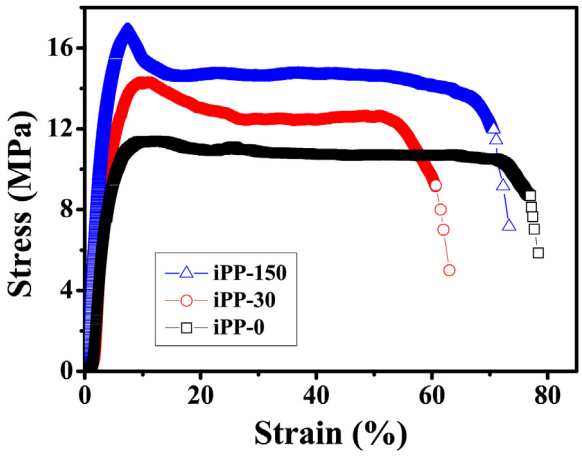

Fig. 11. Typical stress-strain curves of different composite specimens.

ductility and fracture resistance of matrix [5], which can be further confirmed by the following tensile test.

3.5. Influence of interfacial morphology and crystal modification on tensile strength and toughness

In order to further study the effect of interfacial morphology and crystal modification on the interfacial interaction, the representative stress-strain curves of composite specimens after isothermal crystallization for 24 min at 134 °C are shown in Fig. 11. According to the data derived from Fig. 11 (see Table 3), iPP-0 is observed to give the lowest tensile strength of *ca.* 11.25 MPa, and iPP-30 with α-cylindrite has a moderate tensile strength of *ca.* 14.32 MPa, which is

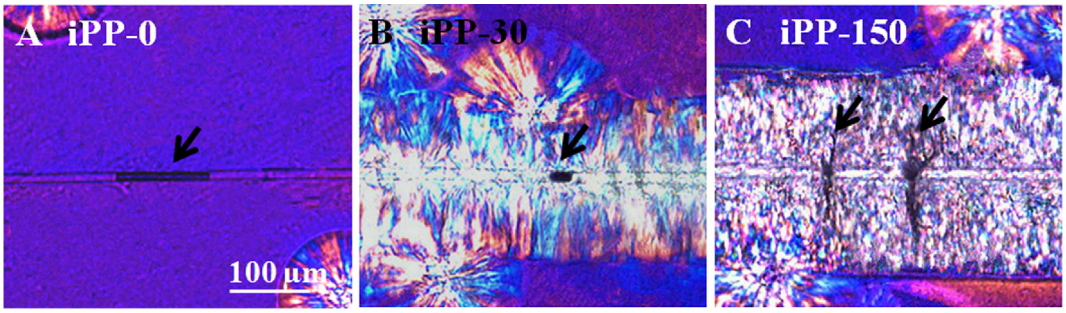

Fig. 10. POM images of stretched fragmentation specimens.

Table 3
Tensile properties of different composite specimens.

Tensile properties	Specimens		
	iPP-0	iPP-30	iPP-150
Tensile strength (MPa)	11.25 ± 0.52	14.32 ± 0.72	16.78 ± 0.81
Elongation at break (%)	78.42 ± 4.70	63.01 ± 3.51	73.35 ± 4.42
Toughness (MJ/m^3)	8.05 ± 0.16	7.45 ± 0.31	10.24 ± 0.47

nearly 1.27 times higher than that of iPP-0. Whereas, iPP-150 with β-cylindrite has the surprisingly highest strength of *ca*. 16.78 MPa, exhibiting an increase of about 49.2% and 17.2% respectively compared with iPP-0 and iPP-30. As proved in the inset of Fig. 6, X_c for all the specimens has no obvious difference. Naturally, different tensile strength should not be ascribed to X_c. Therefore, the reasons to cause enhanced tensile strength should be considered from two main aspects: (1) cylindrite at the iPP/GF interface provides a higher IFSS and improves the load transfer efficiency (see Fig. 9), resulting in higher tensile strength; (2) pulling GF with higher fiber-pulling speed leads to an extended iPP chain with higher orientation level (Fig. 5), which efficiently favors the increment of mechanical properties [46].

As shown in Table 3, the elongation at break of iPP-0, iPP-30 and iPP-150 are around 78.42, 63.01 and 73.35%, respectively. Furthermore, the total mechanical energy per unit volume consumed by the specimen (W_b) when straining it to break is usually used to characterize the toughness of specimen [47]. The higher W_b suggests better toughness, and it can be obtained by integrating the area under stress-strain curves by the following equation: $W_b = \int_0^{\varepsilon} \sigma d\varepsilon$ (ε is the elongation at break). From the calculated results (Table 3), one can see that iPP-150 exhibits the highest toughness (10.24 MJ/m^3), along with an increase of 27.2 and 37.4% compared with iPP-0 (8.05 MJ/m^3) and iPP-30 (7.45 MJ/m^3), respectively. This excellent toughness of iPP-150 should be ascribed to the intrinsic feature of β-form crystal as aforementioned. On the basis of above results, an interesting polymer/fiber composite with balanced tensile strength and toughness could be realized by introducing shear-induced interfacial β-cylindrite.

4. Conclusions

The interfacial shear has significantly influenced the interfacial morphology and crystal modification. α-spherulite, α-cylindrite and β-cylindrite at the interface of iPP/GF composites can be successively induced with increasing the fiber-pulling speed. Furthermore, SFFT and tensile test show that the interfacial interaction is closely related to the morphology and crystal modification of interfacial crystalline layer. Accordingly, the close correlation between interfacial interaction and crystal modification strongly suggests that the interfacial enhancement can be realized by tuning the interfacial crystal modification of iPP-based composites. Especially for the shear-induced β-cylindrite, it opens a new door to produce simultaneously strengthened and toughened iPP-based polymer/fiber composites.

Acknowledgements

The project is financially supported by the National Natural Science Foundation of China (51173171), Major State Basic Research Projects (2012CB025904), Plan for Scientific Innovation Talent of Henan Province and Opening Project of State Key Laboratory of Polymer Materials Engineering (Sichuan University). Z. Guo appreciates the start-up funds from University of Tennessee.

References

[1] N.Y. Ning, S. Fu, W. Zhang, F. Chen, K. Wang, H. Deng, Q. Zhang, Q. Fu, Prog. Polymer Sci. 37 (2012) 1425–1455.
[2] H. Quan, Z.M. Li, M.B. Yang, R. Huang, Compos. Sci. Technol. 65 (2005) 999–1021.
[3] J. Varga, J. Karger-Kocsis, Polymer Bull. 30 (1993) 105–110.
[4] J. Varga, J. Karger-Kocsis, J. Mater. Sci. Lett. 13 (1994) 1069–1071.
[5] S.L. Gao, J.K. Kim, Compos. Part A 31 (2000) 517–530.
[6] C.M. Wu, M. Chen, J. Karger-Kocsis, Polymer 42 (2001) 199–208.
[7] N.E. Zafeiropoulos, C.A. Baillie, J.M. Hodgkinson, Compos. Part A 33 (2002) 1185–1190.
[8] M. Zhou, Y.H. Li, C. He, T.X. Jin, K. Wang, Q. Fu, Compos. Sci. Technol. 91 (2014) 22–29.
[9] F. Hoecker, J. Karger-Kocsis, Polymer Bull. 31 (1993) 707–714.
[10] H. Nuriel, N. Klein, G. Marom, Compos. Sci. Technol. 59 (1996) 1685–1690.
[11] S.J. Han, K. Ren, C.Z. Geng, K. Wang, Q. Zhang, F. Chen, Q. Fu, Polymer Int. 63 (2013) 646–651.
[12] A. Gati, H.D. Wagne, Macromolecules 30 (1997) 3933–3935.
[13] M.J. Folkes, W.K. Wong, Polymer 28 (1987) 1309–1314.
[14] C.M. Wu, M. Chen, J. Karger-Kocsis, Polymer 42 (2001) 129–135.
[15] M.Q. Zhang, J.R. Xu, Z.Y. Zhang, H.M. Zeng, X.D. Xiong, Polymer 37 (1996) 5151–5158.
[16] Y. Zhang, J. Zhang, X.Y. Qian, P. Deng, K.Z. Shen, Polymer 53 (2012) 4318–4327.
[17] T. Asano, Y. Fujiwara, Polymer J. 11 (1979) 383–390.
[18] R.H. Somani, B.S. Hsiao, A. Nogales, H. Fruitwala, S. Srinivas, A.H. Tsou, Macromolecules 34 (2001) 5902–5909.
[19] J. Moitzi, P. Skalicky, Polymer 34 (1993) 3168–3172.
[20] D.G. Gray, J. Polymer Sci. Polymer Lett. 12 (1974) 645–650.
[21] J. Varga, J. Karger-Kocsis, Compos. Sci. Technol. 48 (1993) 191–198.
[22] X.L. Sun, H.H. Li, J. Wang, S.K. Yan, Macromolecules 39 (2006) 8720–8726.
[23] F. Luo, C.Z. Geng, K. Wang, H. Deng, F. Chen, Q. Fu, B. Na, Macromolecules 42 (2009) 9325–9331.
[24] S.C. Zhao, Z. Cai, Z. Xin, Polymer 49 (2008) 2745–2754.
[25] W. Stocker, M. Schumacher, S. Graff, A. Thierry, J.C. Wittmann, B. Lotz, Macromolecules 31 (1998) 807–814.
[26] S.C. Tjong, J.S. Shen, R.K.Y. Li, Polymer Eng. Sci. 36 (1996) 100–105.
[27] B.B. Sun, Y.J. Qin, Y.H. Xu, Y.H. Sun, B. Wang, K. Dai, G.Q. Zheng, C.T. Liu, J.B. Chen, J. Mater. Sci. 48 (2013) 5354–5360.
[28] Y.J. Qin, Y.H. Xu, L.Y. Zhang, G.Q. Zheng, K. Dai, C.T. Liu, X.R. Yan, J. Guo, Z.H. Guo, Polymer 70 (2015) 326–335.
[29] J.L. Thomason, A.A. Van Rooyen, J. Mater. Sci. 27 (1992) 897–907.
[30] H.W. Bai, Y. Wang, Z.J. Zhang, L. Han, Y.L. Li, L. Liu, Z.W. Zhou, Y.F. Men, Macromolecules 42 (2009) 6647–6655.
[31] J. Varga, J. Karger-Kocsis, Polymer 36 (1995) 4877–4881.
[32] X.L. Sun, H.H. Li, I. Lieberwirth, S.K. Yan, Macromolecules 40 (2007) 8244–8249.
[33] J. Varga, J. Karger-Kocsis, J. Polymer Sci. Polymer Phys. 34 (1996) 657–670.
[34] G. Lamberti, V. Brucato, J. Polymer Sci. Polymer Phys. 41 (2003) 998–1008.
[35] F. Sadeghi, A. Ajji, P.J. Carreau, J. Membr. Sci. 292 (2007) 62–71.
[36] F. Sadeghi, P.J. Carreau, Can. J. Chem. Eng. 86 (2008) 1103–1110.
[37] G. Parthasarthy, M. Sevegney, R.M. Kannan, J. Polymer Sci. Polymer Phys. 40 (2002) 2539–2551.
[38] P.C. Painter, M. Watzek, J.L. Koenig, Polymer 18 (1977) 1169–1172.
[39] I.M. Ward, Chapman & Hall, London, 1997.
[40] A. Turner-Jones, J.M. Aizlewood, D.R. Beckett, Makromol. Chem. 75 (1964) 136.
[41] D. Tripathi, F.R. Jones, J. Mater. Sci. 33 (1998) 1–16.
[42] A. Kelly, W.R. Tyson, J. Mech. Phys. Solids 13 (1965) 329–350.
[43] T. Ohsawa, A. Nakayama, M. Miwa, A. Hasegaw, J. Appl. Polymer Sci. 22 (1978) 3203–3212.
[44] J.M. Felix, P. Gatenholm, J. Mater. Sci. 29 (1994) 3043–3049.
[45] E.V. Pisanova, S.F. Zhandarov, Compos. Sci. Technol. 57 (1997) 937–943.
[46] H. Xu, G.J. Zhong, Q. Fu, J. Lei, W. Jiang, B.S. Hsiao, Z.M. Li, ACS Appl. Mater. Interfaces 4 (2012) 6774–6784.
[47] H.W. Hayden, W.G. Moffatt, J. Wulff. Wiley, New York, 1965.